HTML ABSTRACT + LINKS

High power ferromagnetic resonance and spin wave instability processes in Permalloy thin films

Sung Yong An,[a] Pavol Krivosik,[b] Michael A. Kraemer, Heidi M. Olson, Alexey V. Nazarov,[c] and Carl E. Patton
Department of Physics, Colorado State University, Fort Collins, Colorado 80523

(Received 10 February 2004; accepted 28 April 2004)

The high power ferromagnetic resonance (FMR) response, as well as butterfly curves of the spin wave instability threshold microwave field amplitude h_{crit} versus in-plane static field H profiles, have been measured for Permalloy films with thicknesses of 104, 128, and 270 nm at a nominal pumping frequency of 9.37 GHz. The h_{crit} values range from about 1 to 7 Oe. Both the resonance saturation response at the FMR field and the subsidiary absorption (SA) response for static fields below the FMR field are similar in appearance to those for bulk ferrites. Butterfly curves over the SA response region, while similar to those for ferrites, exhibit a film thickness dependent band edge cutoff effect not found in bulk ferrites. The SA butterfly curve data were analyzed on the basis of a spin wave instability theory adapted to thin films. The observed shift in the SA band edge cutoff with thickness agrees with calculations based on the thin film dispersion response and the assumption of first order instability processes with critical modes at one half the pumping frequency. The fitted SA spin wave linewidths give values consistent with metallic relaxation processes, but indicate critical modes with wave vectors that always make relatively small $0°-20°$ angles with the static field, very different from the critical modes for bulk ferrites. Three key conclusions from this work are (1) the nonlinear microwave FMR response in Permalloy films is a threshold effect related to well established spin wave instability processes, (2) the details of the SA response are controlled largely by the thin film spin wave dispersion, and (3) these nonlinear processes occur for very small precession angles. © *2004 American Institute of Physics*. [DOI: 10.1063/1.1763996]

I. INTRODUCTION

Recently, Silva *et al.*[1] have shown that nonlinear effects can play a crucial role in the large angle precession dynamics in magnetic thin films. The data indicated that the initial stages of the large angle precession response to an applied pulsed magnetic field can lead to a reduction in the magnetization of the film over a time scale of several nanoseconds. Even more recently, Nibarger *et al.*[2] have shown that the large as well as small angle free precession magnetization response to pulsed field excitation can be modeled with reasonable accuracy in terms of Landau Lifshitz (LL) damping.

The observation of clear nonlinear effects in precession dynamics, in combination with consistent fits to the large angle decay response with linear damping models, presents a serious dilemma. The nonlinear effects indicate that parametric spin waves are generated at the beginning stages of the response. Early high power microwave ferrite experiments,[3,4] spin wave instability (SWI) theory,[5,6] and high power ferromagnetic resonance (FMR) data for Permalloy films,[7–9] all work from the 1960s, support the magnetization decrease observed in Ref. 1.

At the same time, the good LL damping fits to the large precession angle data indicate that there are no nonlinear damping effects. Many years ago, moreover, Patton and Humphrey [10] also showed that the large angle precession response associated with domain wall motion in Permalloy films could also be modeled through the LL equation with a relatively small value of the LL damping parameter.

One clear way to probe the origin of the nonlinear response in Ref. 1 is to study the FMR response at high power levels. This work is concerned specifically with the resonance saturation (RS) and subsidiary absorption (SA) responses at high power for Permalloy thin films. Measurements of both responses are found to constitute threshold effects consistent with the parametric excitation of spin waves, SWI theory, and nonlinear damping.

Quantitative data were obtained and a theoretical analysis was done for the spin wave instability threshold field amplitude h_{crit} as a function of static field H over the SA field region. With three exceptions, the data follow the general expectations for first and second order SWI processes in bulk ferrites. The exceptions are (1) larger spin wave linewidths consistent with metallic film relaxation mechanisms, (2) a thickness dependent subsidiary absorption band edge, and (3) drastically different critical spin wave modes. The results show clearly that nonlinear spin waves play a critical role in high power precession dynamics.

Section II gives an overview of the film properties and the microwave measurements. Section III presents experimental results on resonance saturation and subsidiary absorp-

[a]Present address: Department of Physics, Kookmin University, Seoul 136-702, Korea.
[b]On leave from the Department of Electromagnetic Field Theory, Faculty of Electrical Engineering and Information Technology, Bratislava, Slovakia.
[c]Present address: Seagate Technology, Bloomington, MN 55435-5489.

 © 2004 American Institute of Physics

Downloaded 06 Sep 2004 to 150.134.221.6. Redistribution subject to AIP license or copyright, see http://jap.aip.org/jap/copyright.jsp

TABLE I. Summary of low power 9.37 GHz ferromagnetic resonance (FMR) measurement results.

Film thickness d (nm)	FMR field H_{res} (Oe)		Half power FMR linewidth ΔH_0 (Oe)		Effective saturation induction $4\pi M_{s\text{-}eff}$ (G)	Gyromagnetic constant $\lvert\gamma\rvert/2\pi$ (MHz/Oe)
	In-plane FMR	Perpendicular-to-plane FMR	In-plane FMR	Perpendicular-to-plane FMR		
104	935	13 560	90	84	10 320	2.89
128	895	13 600	53	58	10.420	2.95
270	910	12 600	82	165	9 520	3.04

tion. Section IV provides an overview of the thin film theory. Section V gives brief SA analysis results. Section VI provides a summary and conclusion.

II. THIN FILM MATERIALS, MICROWAVE MEASUREMENT PROCEDURES, AND FMR CHARACTERIZATION

The Permalloy films were evaporated onto heated glass substrates in a vacuum in the 10^{-6} Torr range. The data below are for circular films with thicknesses of 104, 128, and 270 nm. The 270 nm thickness film was fabricated by Dr. H. Pascard at the Centre Nationale Scientifique Recherche in France and had a nominal composition of 83 at.% Ni and 17 at.% Fe. This film was similar to those used for the work cited above in Ref. 7. The 104 and 128 nm thick films with nominal compositions of 80 at.% Ni and 20 at. % Fe were made by Dr. F. Ono at Tohoku University, Sendai, Japan and previously used for the effective linewidth work reported in Ref. 11. These available films and this range of thicknesses provided a representative map of the different high power responses that can be obtained for thin films. In spite of the fact that these films are over 30 years old, they all exhibited clean and reasonably narrow FMR lines. The low power FMR data are considered below.

The microwave measurements were made for both in-plane and perpendicular-to-plane static fields, with the linearly polarized microwave excitation always in-plane and perpendicular to the static field. The low and high power measurements were made with a pulsed microwave reflection cavity spectrometer system similar to that described in Refs. 12 and 13. The data were obtained with 50 μs wide pulses, a repetition rate of 40 Hz, and peak power levels up to 1 kW.

The empty cavity had a nominal resonance frequence f_p of 9.37 GHz, a power reflection coefficient of −12 dB at cavity resonance, and a loaded Q of 2100. The cavity was undercoupled and had a calibration coefficient $C=h^2/P$ relating the microwave field amplitude h to the cavity input power P of 2.6 Oe^2/W. The calibration factor C can be applied to the SA response because of the small effect of the sample on the cavity parameters far off resonance. It cannot be applied to the RS response because of the strong absorption in the vicinity of ferromagnetic resonance and the substantial drop in the cavity Q, typically by 30%–40% at the FMR peak. For this reason, the quantitative data and analyses for this report were confined to the SA response. Further RS work is underway.

The measurement system was operated under computer control with LABVIEW® software. For the low power FMR measurements, the static field was stepped in small increments, the cavity frequency was tuned to resonance at each field point, and the power reflection coefficient was measured. The high power measurements were done in two ways. In the first, the cavity reflection coefficient was measured as a function of static field for a wide range of peak powers. The field scan was extended to low fields to capture the SA response. In the second, the static field was held fixed at different values over the scan range used above and the reflection coefficient was measured as a function of the microwave power level in the cavity. These data generally showed threshold responses. After conversion to plots of loss versus microwave field amplitude h, these plots were used to determine values of the microwave field SWI threshold amplitude h_{crit} at each field point. The accuracy of the h_{crit} determinations was about 15%. These data were then used to obtain plots of h_{crit} versus static field H, so-called "butterfly curves." The high power data given below are limited to the in-plane field configuration.

Table I summarizes the low power FMR measurement results. The values of the effective saturation induction $4\pi M_{s\text{-}eff}$ and the gyromagnetic constant $\lvert\gamma\rvert/2\pi$ were determined from the FMR field H_{res} values in the in-plane and perpendicular-to-plane field configurations. Small surface anisotropy effects make $4\pi M_{s\text{-}eff}$ slightly different from the actual saturation induction, $4\pi M_s$. The $4\pi M_{s\text{-}eff}$ and $\lvert\gamma\rvert/2\pi$ values will be used for the SA computations in Secs. III–V. The FMR linewidths are slightly larger than the typical values for low loss Permalloy films. This indicates possible inhomogeneity scattering and, in for the 270 nm film, eddy-current losses. These linewidth contributions, however, do not affect the SWI processes in a significant manner. The results in Table I and the analysis in the rest of this paper use Gaussian cgs units.

III. HIGH POWER FERROMAGNETIC RESONANCE AND SUBSIDIARY ABSORPTION RESPONSE

A. Microwave response at high power

Figure 1 shows the effect of high power on the FMR absorption profile and the loss for fields below the FMR peak. The solid and open circle data show the uncalibrated microwave loss for the 128 nm film as a function of the static external magnetic field H for a cavity input peak pulse power P of 7.6 mW and 40.5 W, respectively. The icon shows the field configuration. The RS and SA labels indicate, respectively, the resonance saturation and subsidiary absorption regions.

Downloaded 06 Sep 2004 to 150.134.221.6. Redistribution subject to AIP license or copyright, see http://jap.aip.org/jap/copyright.jsp

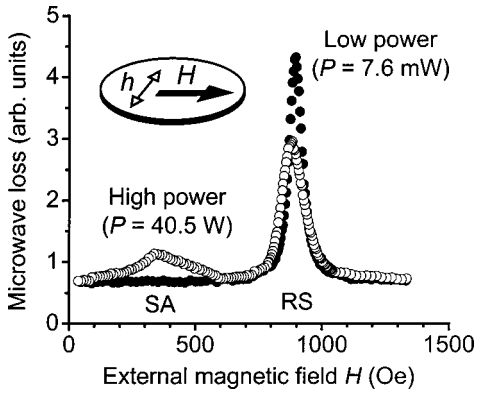

FIG. 1. Microwave loss vs the static external magnetic field H for the 128 nm thick film for the in-plane static field configuration and pulse microwave excitation at 9.37 GHz. Both **H** and the orthogonal linearly polarized microwave field **h** were in plane, as indicated. The solid and open circles denote data for a peak input power P to the cavity of 7.6 mW and 40.5 W, respectively. The RS and SA labels indicate the field regions for resonance saturation and subsidiary absorption, respectively.

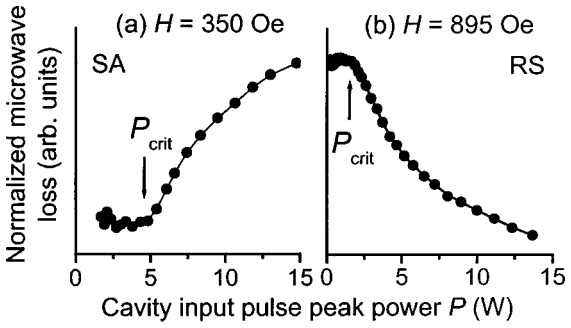

FIG. 2. Microwave loss vs cavity input pulse peak power P for the 128 nm Permalloy film at 9.37 GHz with the static field H and the orthogonal microwave field both in plane. The H values were as indicated. Graph (a) shows a typical subsidiary absorption (SA) response. Graph (b) shows resonance saturation (RS). The vertical arrows and the P_{crit} labels indicate the powers at the spin wave instability threshold points.

The Fig. 1 data demonstrate the basic high power effects. The FMR peak position at 895 Oe and the nominal half power linewidth of 53 Oe correspond to the expected low power FMR response for a thin Permalloy film. When the input power is increased and the amplitude of the microwave magnetic field becomes large, the FMR absorption curve broadens and the peak absorption level drops. This is the resonance saturation or RS response. High power also leads to a somewhat broad and lower power SA peak for fields well below the main FMR peak. Note that the two data sets in Fig. 1 are for input powers that differ by a factor of about 5×10^3 and, hence, for microwave field amplitudes that differ by about a factor of 70.

The RS and SA responses in Fig. 1 are similar to the high power effects found for ferrite materials. Reviews of these effects may be found in Refs. 14 and 15, and in a recent theoretical paper by Nazarov *et al.*[16] There are several signatures that show that these responses are "nonclassical," in the sense that nonlinear spin wave processes are involved. First, the RS response occurs for power levels *well below* those for which a classical nonlinear broadening is expected. Second, there is no way to obtain a low field high power SA loss peak of the sort shown in Fig. 1 from purely classical considerations. Both effects are related to the parametric excitation of spin waves. The high power responses in Fig. 1 are actually threshold effects. Both responses occur abruptly at some critical power level as the power is increased. These are *not* gradual incremental effects.

Figure 2 shows representative data on these threshold responses. Both panels show microwave loss as a function of the cavity input pulse peak power P for the in-plane static field configuration. Graph (a) is for $H=350$ Oe, just at the peak of the SA response in Fig. 1. The RS response in graph (b) is for $H=895$ Oe, a field point close to the low power FMR peak position. The vertical arrows and the P_{crit} labels indicate the threshold power points in the graphs.

The threshold nature of the response is clear from both graphs in Fig. 2. In graph (a), the microwave loss level is extremely low for power levels below the $P\approx P_{crit}$ point. The loss increases sharply as P goes above this level and the SA response develops accordingly. Keep in mind that for the SA response, one is on the extreme low field FMR tail. The threshold power level at this point corresponds to the microwave field amplitude of about 3.5 Oe. As the SA response develops for $P>P_{crit}$, the low losses associated with this tail response change abruptly into high losses. For the RS response in (b), one sees the opposite effect. Here, one has high losses for $P<P_{crit}$ that *drop abruptly* as the power goes above the threshold point.

The threshold responses shown in Fig. 2 provide the basis for an explanation through the parametric spin wave instability theory developed by Suhl and Schloemann for bulk ferrites. The SA threshold response in (a) occurs only for a limited field range for which spin waves are available at *one half* the pumping frequency. The control parameters that determine the upper cutoff field for this type of threshold response include the frequency, magnetization, and film thickness. These factors will be considered shortly. The two important points here are that (1) these effects occur for static fields *very far* from ferromagnetic resonance and (2), the magnetization precession angle for this low field tail is extremely small.

The RS response in Fig. 2(b) is due to the parametric excitation of spin waves at frequencies *equal to* the pump frequency. The actual threshold is tied closely to the low power FMR precession amplitude. The corresponding P_{crit} is usually the smallest at the FMR peak where the precession angle is the largest. Based on the threshold P_{crit} point in graph (b) and the empty cavity calibration factor of 2.6 Oe^2/W, the estimated magnetization precession cone angle at the threshold is in the range of a few degrees. This means that spin wave instability at the FMR peak also occurs for relatively small precession angles.

B. Subsidiary absorption butterfly curves

Figure 3 shows representative SA butterfly curves of the threshold microwave field amplitude h_{crit} as a function of the static field H for the three films in the in-plane configuration, as indicated. These threshold fields were obtained from data similar to those in Fig. 2(a) over the range of static field values indicated, along with the cavity calibration given

Downloaded 06 Sep 2004 to 150.134.221.6. Redistribution subject to AIP license or copyright, see http://jap.aip.org/jap/copyright.jsp

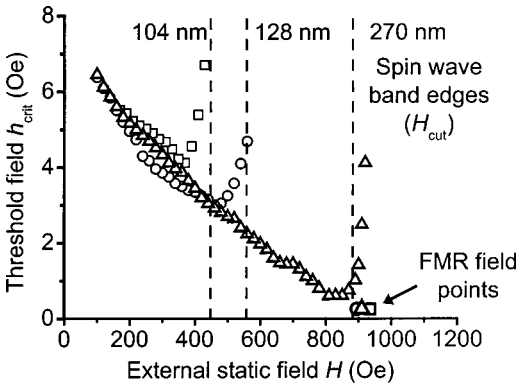

FIG. 3. Butterfly curves of the spin wave instability threshold microwave field amplitude h_{crit} vs static external magnetic field H for the subsidiary absorption responses in the three different thickness films, as indicated. These data are for the in-plane static field configuration. The h_{crit} points were obtained from data similar to those in Fig. 2(a) and the empty cavity power-field calibration given in text. The vertical dashed lines indicate values of the computed cutoff static field H_{cut} for half frequency spin waves for the three films, as indicated. The open bold symbols indicate the FMR field positions for the three films.

above. Because of the low cavity loading in the SA field region that is generally well below FMR, this calibration is reasonably accurate. Due to the increased loading for fields close to FMR, the calibration is not particularly good for fields above about 800 Oe. This means that the actual h_{crit} values for the 270 nm film at the upper end of the data range are somewhat different than those indicated in the figure. The vertical dashed lines in Fig. 3 show computed half frequency spin wave cutoff field values for the films, as indicated. These fields correspond to the points at which spin waves at one half the pump frequency of 9.37 GHz cease to be available for parametric excitation. The bold open symbols indicate the FMR field points from Table I. The FMR symbol shapes track those for the butterfly curves.

The butterfly curves in Fig. 3 are similar in appearance to those for ferrite materials. The curves show minimum h_{crit} values at some field H_{min} close to the peak in the SA absorption response. These minimum threshold values range from about 4 Oe for the 104 nm thick film, down to about 0.5 Oe for $d=270$ nm. The h_{crit} values for $H<H_{min}$ tend to increase as H extends farther and farther below H_{min}. These portions of the data for the three films, moreover, appear to lie on a common line. For fields above H_{min} for each film, the h_{crit} values also increase as one moves away from the minimum point. These thresholds appear to diverge as one approaches a high field cutoff point at some H_{cut} and show a band edge effect.

There are also differences. The data show, for example, that the entire butterfly curves, as well as the H_{cut} points, shift to higher fields as the film thickness is increased. There is no comparable effect for butterfly curves in bulk ferrites. The cutoff field points shown by the dashed lines match reasonably to the divergence points evident from the data for the 104 and 128 nm thick films, and that these points lie well below the corresponding FMR fields. For $d=270$ nm, however, the h_{crit} values extend slightly above the FMR point and a computed H_{cut} that is slightly below the FMR field. These observations will be important in Sec. V.

The above responses are tied closely to the nature of the spin wave dispersion curves for thin films, and more specifically, the way in which the spin wave modes change with film thickness, the wave vector **k**-dependent spin wave relaxation rate $\eta_k(\mathbf{k})$ for these modes, and the coupling of the half frequency spin wave modes to the FMR uniform mode precession response. It is the excitation of *minimum threshold critical modes* that gives rise to the threshold responses evident in Fig. 3. The shift in the H_{min} and H_{cut} points with thickness have to do with changes in the bottom of the spin wave band with film thickness. The rise in h_{crit} for $H<H_{min}$ is explicitly related to a **k**-dependent spin wave relaxation rate η_k. The theoretical analysis in Sec. IV and fits to the data in Sec. V will demonstrate these effects.

IV. SPIN WAVE INSTABILITY ANALYSIS

A. Theory basics

General SWI theories for bulk and thin film samples may be found in Refs. 16 and 17, respectively. Reference 17 considered SA and the related parallel pumping process only. For the present purposes, a somewhat simpler SWI analysis has been developed to analyze thin film data over the full range of static fields and pumping configurations for both RS and SA processes. The formulation is based on the well established work of Suhl[5] and Schloemann.[6] It follows the effective field approach given in Ref. 18, but adapted to the thin film geometry. It is assumed that the film is thin enough for the dynamic magnetization response for the spin wave modes to be taken as uniform over the film cross section.[19–21] This approximation corresponds to the lowest order mode analysis in Ref. 17.

The uniform spin wave mode approximation is reasonable for very thin films. Among other things, spin waves with a nonuniform dynamic response over the film cross section will have frequencies that are exchange shifted well above the frequencies of interest. The smooth butterfly curve profiles in Fig. 3 and the lack of any evident spin wave mode related structure support the use of this approximation. Butterfly curves for thicker films, in contrast, show considerable structure that is attributed to jumps between different dipole-exchange dispersion branches.[17,22] The uniform dynamic response approximation also makes an analytic theory tractable. Without these simplifications, a general nonlocal exchange analysis through numerical methods[23] or a Green's function approach[24] is needed.

The analysis starts with a Fourier expansion of the dynamic magnetization $\mathbf{m}(\mathbf{r},t)$ of the form

$$\mathbf{m}(\mathbf{r},t)=\mathbf{m}_0 e^{i\omega_p t}+\sum_{k\neq 0}\mathbf{m}_k(t)e^{-i(\mathbf{k}\cdot\mathbf{r}-\omega_k t)}, \tag{1}$$

where $\mathbf{m}_0$ is the amplitude of the uniform mode response at the pumping frequency ω_p, the $\mathbf{m}_k(t)$ are Fourier component quasiplane wave amplitudes for spin waves with an in-plane wave vector $\mathbf{k}=k_x\hat{\mathbf{x}}+k_z\hat{\mathbf{z}}$ and frequency ω_k. The film plane is the x-z plane, the film is saturated in the z direction by a static field $\mathbf{H}=H\hat{\mathbf{z}}$, and a linearly polarized microwave field of amplitude h is applied along the x direction. One then makes a similar expansion of the dynamic dipolar field and

Downloaded 06 Sep 2004 to 150.134.221.6. Redistribution subject to AIP license or copyright, see http://jap.aip.org/jap/copyright.jsp

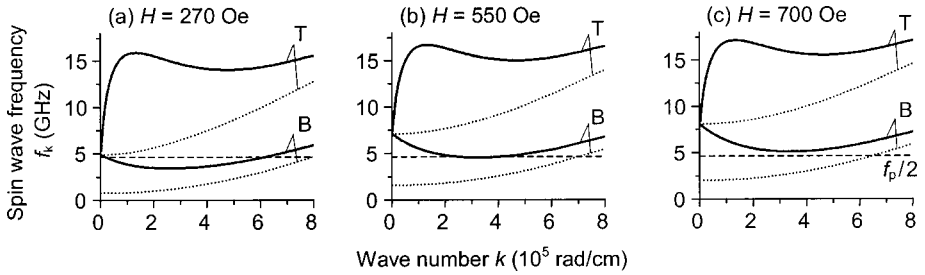

FIG. 4. Thin film and bulk spin wave frequency f_k as a function of wave number k for a 128 nm Permalloy film and three values of the static in-plane field H. The upper and lower solid curves are for in-plane wave vectors perpendicular or parallel to the field, respectively. These curves define the top (T) and bottom (B) of the thin film spin wave bands, as indicated. The dotted curves show the corresponding bulk spin wave band limits. The horizontal dashed lines mark the frequency $f_k=f_p/2=4.68$ GHz at one half the experimental pump frequency f_p.

substitutes both expansions into the torque equation of motion.

The above procedure yields a set of nonlinear coupled algebraic equations in $\mathbf{m}_0$ and the $\mathbf{m}_k$ amplitudes. If one then retains only the linear terms in the $\mathbf{m}_k$, a series of transformations leads to the thin film spin wave $\omega_k(\mathbf{k})$ dispersion. If the analysis is extended to include higher order terms in the uniform mode amplitude $\mathbf{m}_0$, one obtains an instability condition for the exponential growth in time of the $\mathbf{m}_k$ amplitudes for some threshold value h_c of the microwave field amplitude h. This threshold will be a function of $\mathbf{k}$ and ω_k. The threshold $h_{\rm crit}$ that is found experimentally for a given H corresponds to the minimum threshold among all allowed spin wave modes. For the subsidiary absorption range of fields considered here, this $h_{\rm crit}$ occurs for spin wave modes at $\omega_k=\omega_p/2$ and some critical mode wave number value $k_{\rm crit}$ and propagation angle $\theta_{\rm crit}=\tan^{-1}[(\mathbf{k}_{\rm crit})_x/(\mathbf{k}_{\rm crit})_z]$. For the discussion below, the symbol ω will generally be used to denote angular frequency in rad/s, while f will be used for frequencies in GHz.

B. Spin wave dispersion and available modes

The above analysis gives a thin film $\omega_k(\mathbf{k})$ dispersion relation of the form

$$\omega_k=|\gamma|\{[H+Dk^2+4\pi M_s(1-N_k)\sin^2\theta_k] \times[H+Dk^2+4\pi M_s N_k]\}^{1/2}, \quad (2)$$

where M_s is saturation magnetization, D is exchange constant, θ_k is the angle between the in-plane wave vector $\mathbf{k}$ and the in-plane static field $\mathbf{H}$. The N_k represents an effective demagnetizing factor equal to $(1-e^{-kd})/kd$, where $k=|\mathbf{k}|$ and d is the film thickness.[19] Equation (2) corresponds to the spin wave dispersion for the lowest order noninteracting spin wave mode.[17] As a point of reference, the spin wave dispersion in the bulk limit for isotropic ferromagnets is given by

$$\omega_k=|\gamma|\{[H+Dk^2+4\pi M_s\sin^2\theta_k][H+Dk^2]\}^{1/2}, \quad (3)$$

where H is now the internal static field and θ_k denotes the unconstrained polar angle between the wave vector $\mathbf{k}$ and the static field direction. Equation (3) has the same form as Eq. (2) in the $kd\to\infty$ and $N_k\to 0$ limits, except that $\mathbf{k}$ is no longer constrained to the film plane.

Figure 4 shows the thin film and bulk spin wave dispersion curves of frequency $f_k=\omega_k/2\pi$ versus k. The solid thin film curves are based on Eq. (2) for a 128 nm thick film. The dotted bulk curves are based on Eq. (3). The (a), (b), and (c) graphs are for three selected values of the external static field H, as indicated. The graphs show dispersion curves for the bottom of the spin wave band at $\theta_k=0$, labeled B, and the top of the band at $\theta_k=90°$, labeled T. The dispersion curves were all obtained for $|\gamma|/2\pi=2.95$ MHz/Oe, $4\pi M_s=10\,420$ G, and $D=2.1\times10^{-9}$ Oe cm^2/rad^2. The graphs also show a common horizontal dashed line that threads all of the graphs at $f_k=f_p/2=4.68$ GHz, one half of the nominal pumping frequency for the data in Sec. III.

Note that the total thin film or bulk spin wave bands occupy the (k,f_k) regions enclosed by the corresponding limit curves. The $|\gamma|$ and $4\pi M_s$ values for the computations come from the low power FMR results in Table I. The D value is typical of exchange stiffness parameters obtained from standing spin wave resonance experiments in Permalloy.[25] This particular value was estimated from the butterfly curve analysis to be considered in Secs. IV C and V.

The field values for the three graphs in Fig. 4 were selected to show how the shift in the spin wave band with field, relative to the half frequency $f_p/2$ line, affects the available modes at this frequency. Graph (a) is for an H value well below the band edge line for the 128 nm film in Fig. 3, (b) is for a field close to the cutoff value, and (c) is for an H well above this point. For (a), there is a sizeable range of available spin wave modes at $f_k=f_p/2$ with k values from relatively small values up to about 6×10^5 rad/cm. As one moves up to $H=558$ Oe, the bottom of the band moves up in frequency and the range of available k values at $f_k=f_p/2$ shrinks to include only values of 3×10^5 rad/cm or so. At the band edge point for $H=558$ Oe, the width of this k region drops to zero. For higher fields, as in (c), there are no available modes at $f_k=f_p/2$.

The shifts in the bottom band edge for the thin film spin wave dispersion with field in Fig. 4, along with the corresponding changes in the available modes at $f_p/2$, are tied directly to the butterfly curve response for the 128 nm film in Fig. 3. The most obvious connection is with the cutoff field point above which there are no available modes at $f_p/2$. In general, this $H_{\rm cut}$ field is the H value from Eq. (2) at which the minimum in the f_k versus k curve for $\theta_k=0$ rises above the $f_k=f_p/2$ line in Fig. 4. The H value for Fig. 4(b) is set just close to this cutoff point $H=558$ Oe which matches the vertical $H_{\rm cut}$ line in Fig. 3 for 128 nm.

Downloaded 06 Sep 2004 to 150.134.221.6. Redistribution subject to AIP license or copyright, see http://jap.aip.org/jap/copyright.jsp

C. Critical modes and threshold microwave field amplitudes

The Suhl/Schloemann type of analysis outlined above leads to a time dependent m_k amplitude of the form

$$m_k(t) = m_{k0} e^{[-\eta_k + \sqrt{|G_k^{(n)}|^2 - (\omega_k - n\omega_p/2)^2}]t} = m_{k0} e^{\beta_k^{(n)} t}, \tag{4}$$

where m_{k0} is some thermal amplitude, η_k is the spin wave relaxation rate, $G_k^{(n)}$ is a complex ω_k-, k-, θ_k-, and h-dependent coupling coefficient that increases with h, and n is an index that can range over all positive and negative integers. The full square bracket exponential factor constitutes the increment $\beta_k^{(n)}$ for the onset of the nonlinear response. For $\beta_k^{(n)} < 0$, one has an exponential decay response and the m_k reside at thermal levels. As h is increased, $G_k^{(n)}$ also increases. When $G_k^{(n)}$ for a given n is at the $\beta_k^{(n)} = 0$ point, the corresponding h represents the SWI threshold for the particular (ω_k, k, θ_k) mode under consideration.

The h_{crit} at a given static field H and pumping frequency f_p is obtained as the *minimum* threshold among all available (ω_k, k, θ_k) modes under these conditions. From Eq. (4), one can see that for $n=1$, the threshold will occur for $\omega_k = \omega_p/2$ and the (ω_k, k, θ_k) mode that satisfies $|G_k^{(1)}| = \eta_k$ for the the smallest possible value of the microwave field amplitude h. Note that the $G_k^{(1)}$ coupling factor also contains the microwave field h to the first power, and this is the origin of the "first order process" label. For $n=2$, the threshold will be for $\omega_k = \omega_p$ and the (ω_k, k, θ_k) mode that satisfies $|G_k^{(2)}| = \eta_k$ for the smallest possible h. The $G_k^{(2)}$ coefficient, however, scales as h^2. This is the origin of the "second order process" label. It is important to emphasize that the observed threshold in each case will correspond to the critical modes for the particular **k** values that give the smallest h_{crit}.

It is important to keep in mind that the spin wave band shifts with field, as in Fig. 4. This means that the range of available modes at $\omega_k = \omega_p/2$ for first order processes, and for the modes at $\omega_k = \omega_p$ for second order processes, also shifts with field. Because of this band shift with field, the field regimes over which spin waves at $\omega_k = \omega_p/2$, as needed for a first order instability, or at $\omega_k = \omega_p$, as needed for a second order process, can be quite different. Figure 4 shows, for example, that the bottom portion of the spin wave band will pass through the $\omega_k = \omega_p/2$ frequency cut for a range of fields in the 200–600 Oe range. The broad SA peak in Fig. 2 and the butterfly curves in Fig. 3 reflect the availability of these modes for first order instability. One can also see from Fig. 4 that considerably higher fields are needed to push the bottom of the band up to a cut at $\omega_k = \omega_p$. The range of fields for this band position is the same as for ferromagnetic resonance. The remaining discussion here will be for $G_k^{(1)}$ and first order processes.

It proves convenient to write $G_k^{(1)}$ in the form

$$G_k^{(1)}(k, \theta_k) = \frac{|\gamma| h \omega_M}{2\omega_p} W_k^{(1)}(k, \theta_k), \tag{5}$$

where the dimensionless $W_k^{(1)}(k, \theta_k)$ function separates out all of the k and θ_k dependences in $G_k^{(1)}$. This form also separates out the linear h factor and the denominator frequency term. Note that this denominator has already folded in the $\omega_k = \omega_p/2$ condition for first order processes. The ω_M parameter is equal to $|\gamma| 4\pi M_s$ and simply expresses the saturation induction in frequency units. The allowed k and θ_k values in each case come from the spin wave dispersion relation in Eq. (2) and the $\omega_k = \omega_p/2$ constraint. The values of k and θ_k that satisfy the $|G_k^{(1)}| = \eta_k$ condition for the smallest possible h value will correspond to the critical modes and the minimum h value will correspond to h_{crit}. The $W_k^{(1)}(k, \theta_k)$ function is given in the Appendix.

Based on the above, one can write a simple working expression for the first order h_{crit}

$$h_{\text{crit}}^{(1)} = \frac{\omega_p}{\omega_M} \min \left[\frac{\Delta H_k(k, \theta_k)}{|W_k^{(1)}(k, \theta_k)|} \right]_{\omega_k = \omega_p/2}^{k, \theta_k}. \tag{6}$$

Equation (6) contains one new parameter, the so-called "spin wave linewidth" parameter $\Delta H_k(k, \theta_k)$. This parameter is used to express the relaxation rate η_k in linewidth units according to $\Delta H_k = 2\eta_k/|\gamma|$. This form is particularly convenient for rough comparisons with FMR linewidths. The low power FMR linewidth for samples with rotational symmetry about the static field is equal to $2\eta_0/|\gamma|$, where η_0 is the corresponding uniform mode relaxation rate. As with $G_k^{(1)}(k, \theta_k)$ and $W_k^{(1)}(k, \theta_k)$, k and θ_k dependences are shown explicitly to account for any possible **k** dependences.

The operational procedure for butterfly curve calculations and fits to the data is given in Ref. 16. (1) One assumes a trial function for $\Delta H_k(k, \theta_k)$. (2) One determines the range of available spin wave k and θ_k states at $\omega_k = \omega_p/2$ for a given H value. (3) One applies Eq. (6), scans over the available states, and determines the minimum h_{crit} for that H value. (4) A repeat of steps (2) and (3) for the full range of butterfly curve H values then yields a plot of h_{crit} versus H, as well as a map of the corresponding critical mode k and θ_k values. (5) One may then go back to step (1), modify the $\Delta H_k(k, \theta_k)$ trial function, and seek improvements in the match with the data.

V. NUMERICAL EVALUATIONS—CUTOFF FIELDS, BUTTERFLY CURVES AND CRITICAL MODES, AND SPIN WAVE LINEWIDTHS

Figure 5 shows two sets of computed SA butterfly curves for first order processes, along with companion data from Fig. 3. The solid lines show the computed curves and the open points show the data. Film thicknesses are as indicated. The computations were based on a spin wave linewidth of the form $\Delta H_k = A + B \sin^2 2\theta_k$. The curves in graph (a) were obtained for a single and **k**-independent spin wave linewidth with $B=0$. The common A value was adjusted to give the best overall fit to the high field parts of the three data sets. The curves in (b) were obtained for different A values for each film and nonzero B values, in order to fit the low field regions of the butterfly curves as well. Along with these A and B adjustments, the values of the exchange stiffness parameter D for the three films were also optimized to give the best fits. The applicable values are listed in Table II. The $4\pi M_s$, $|\gamma|$, and η_0 parameters needed for the computations were taken from the FMR results in Table I, with $4\pi M_s$

Downloaded 06 Sep 2004 to 150.134.221.6. Redistribution subject to AIP license or copyright, see http://jap.aip.org/jap/copyright.jsp

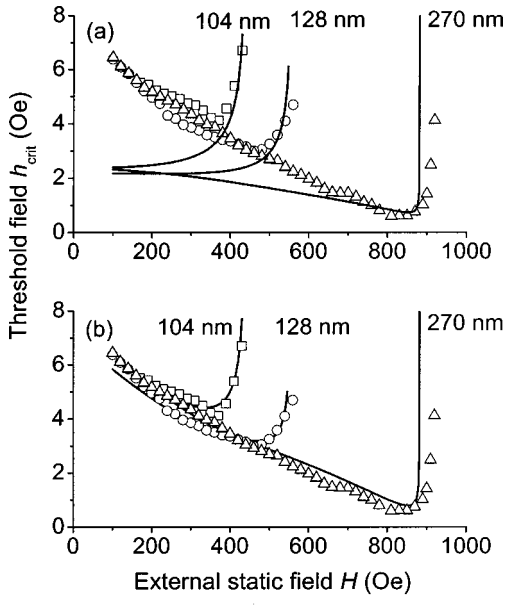

FIG. 5. Butterfly curves of the spin wave instability threshold microwave field amplitude h_{crit} vs static external magnetic field H for the subsidiary absorption responses in the three different thickness films, as indicated. The open symbols show the data from Fig. 3. The solid lines show computed curves for first order processes. The curves in (a) are for a constant spin wave linewidth ΔH_k of 12 Oe. The curves in (b) are for $\Delta H_k = A + B \sin^2 2\theta_k$, where k is the wave number and θ_k is the in-plane propagation angle relative the fields. The A and B parameters, as well as the exchange parameter D were optimized film by film for best fits to the data. The parameters values are listed in Table II.

taken from the listed $4\pi M_{s\text{-eff}}$ results and η_0 obtained from the parallel linewidth and Eq. (A6) from the Appendix.

The results in Fig. 5 show that the Suhl/Schloemann subsidiary absorption spin wave instability analysis, suitably modified, can provide a reasonable match to measured SA butterfly curves for Permalloy thin films. Graph (a) shows that a constant ΔH_k is sufficient to match the high field portions of the theoretical response to the data. The band edge effect at $H = H_{cut}$ is also evident in the computed curves.

Graph (b), moreover, shows that the addition of a relatively simple $\sin^2 2\theta_k$ term to the spin wave linewidth function allows one to match the low field parts of the computed curves to the data as well. It is important to note at this point that the values of the A and B parameters for the fits in Fig. 5(b) are all reasonable values for Permalloy. Based on the 9.37 GHz FMR in-plane linewidth values in Table I, the scaled linewidths at $f_k = f_p/2$ would be in the range of 26–45 Oe. With the critical mode properties taken into account, the A and B values in Table II give linewidths in this range. Critical modes will be considered shortly.

The $\Delta H_k = A + B \sin^2 2\theta_k$ trial spin wave linewidth function is similar to that needed to obtain good fits to butterfly curve data for ferrites. Ferrites generally require a spin wave linewidth of the form $\Delta H_k = A' + B' \sin^2 2\theta_k + C' L(k)$, where the $L(k)$ function gives something between a linear and a step response in k to account for three magnon relaxation.[26] The success of a closely related function for metallic films is intriguing, since the physical relaxation mechanisms are known to be quite different. The roles of the A and the B terms in the actual fits are also quite different. For ferrites, one generally needs a $\sin^2 2\theta_k$ response to fit the high field parts of the butterfly curves and the constant and k-dependent terms to fit the low field regions.[15] For these metallic films, the $\sin^2 2\theta_k$ term is needed for the low field regions and the constant term gives a good high field match.

It is also noteworthy that the *worst* fits in Fig. 5 are for the high field parts of the butterfly curve for 270 nm thick film. The fits are poor and, as evident in Fig. 3, the h_{crit} data extend to higher fields that are well above the computed band edge H_{cut} limit. There is also the experimental problem of cavity overloading for fields close to the FMR point, and actual h_{crit} values that are lower than those shown in Figs. 3 and 5. Further experimental and theoretical work is needed here.

Recall that the computed $h_{crit}(H)$ responses in Fig. 5 are accompanied by critical mode (CM) wave number $k(H)$ and propagation angle $\theta_k(H)$ profiles. Figure 6 shows these companion profiles. Graphs (a) and (b) show the individual $k(H)$ and $\theta_k(H)$ CM responses, respectively, for the 128 nm film. The vertical dashed lines mark the corresponding SA cutoff field H_{cut} point from Fig. 3 for the 128 nm film. Graph (c) shows the CM response profiles in polar form for all three films, as indicated. For clarity, the profiles in graph (c) are shown with symbols instead of curves. The symbols match those used for the data for the three films in Figs. 3 and 5.

Figure 6 shows three main regions. (1) At low fields, below 250 Oe or so, the CM wave number k sticks at a nearly constant value that decreases with increasing thickness from about 1.8×10^5 rad/cm for $d = 104$ nm to about 0.6×10^5 rad/cm for $d = 270$ nm. This flat k response is accompanied by a nearly linear decrease in the CM θ_k from about 20° down to 10° or so. (2) There is then an intermediate field range over which the CM θ_k decreases more

TABLE II. Summary of parameters for the optimized fits to the subsidiary absorption butterfly curve data in Fig. 5.

Film thickness d(nm)	Exchange coefficient D(Oe cm^2/rad^2)	Spin wave linewidth parameters in the $\Delta H_k = A + B \sin^2 2\theta_k$ function (in Oe)		
	Graphs (a) and (b)	Graph (a)	Graph (b)	
		A	A	B
104	2.7×10^{-9}	12	12	80
128	2.1×10^{-9}	12	10	90
270	2.0×10^{-9}	12	9	80

Downloaded 06 Sep 2004 to 150.134.221.6. Redistribution subject to AIP license or copyright, see http://jap.aip.org/jap/copyright.jsp

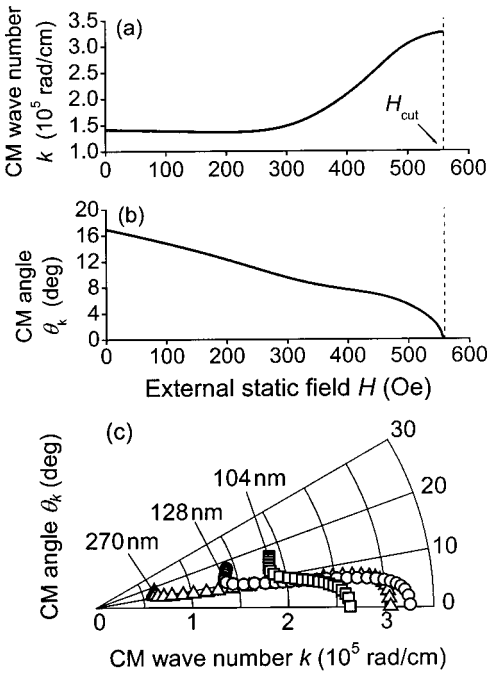

FIG. 6. Graphs (a) and (b) show the critical mode (CM) wave number k and propagation angle θ_k, respectively, as a function of the external static field H that accompany the computed threshold field $h_{crit}(H)$ subsidiary absorption (SA) response in Fig. 5 for the 128 nm film. The vertical dashed lines show the corresponding SA cutoff field H_{cut} point from Fig. 3. Graph (c) shows combined CM results in polar form for all three films, as indicated.

slowly and the CM k values increase rapidly as the field is increased. (3) Finally, as H approaches the H_{cut} point for each thickness, the CM θ_k goes to zero and the CM k value moves to the minimum point on the corresponding bottom-of-the-band dispersion curve in Fig. 4.

Even though the butterfly curves in Figs. 3 and 5 are similar in appearance to those for bulk ferrite materials, the corresponding critical mode profiles are quite different. In typical bulk ferrite samples, the CM k decreases smoothly to zero at a field point close to the butterfly curve minimum and then sticks at zero up to the cutoff. At the same time, the CM θ_k sticks at some value close to about 45° for fields below the minimum h_{crit} point, and then drops smoothly to zero. The Permalloy film CM profiles are quite the opposite. These drastic differences can be explained by (1) the very high M_s in Permalloy relative to ferrites, (2) the very different nature of the spin wave band because of both thin film geometry and high magnetization, and (3) the different k and θ_k dependences for the W_k coupling factor. The main points, briefly stated, involve (1) the availability of two different k values for a specific θ_k along a given frequency cut at $\omega_k = \omega_p/2$, (2) a general preference for the lower k value for the critical mode because of the higher ellipticity of the precession cone for that particular spin wave, (3) different three magnon scattering selection rules for thin films relative to bulk. A full discussion will be given in a follow-up theory paper.

VI. SUMMARY AND CONCLUSION

The effect of high power on the ferromagnetic resonance response in a series of thin Permalloy films has been examined experimentally and theoretically. The threshold nature of the high power response has been verified for both resonance saturation and the broad subsidiary absorption (SA) peak for a range of fields below the FMR peak. Quantitative measurements of the actual threshold microwave field amplitudes versus field, so-called butterfly curves, were also made. Upper limit cutoff fields for the SA response shift up with film thickness and match precisely to the field point at which the bottom of the spin wave band moves above one half the pump frequency. All of these responses show that there are clear and definitive spin wave instability effects for relatively low FMR precession angles and for extremely small precession angles in the SA response region.

A new and relatively simple theoretical analysis of spin wave instability (SWI) processes in thin films has been developed, based on the Suhl/Schloemann SWI formalism for bulk ferrites but suitably modified for the thin films. The theory has been used to fit the experimental butterfly curves and extract operational formulas for the spin wave linewidth in these metallic thin films. The numerical values of the fitted linewidths are close to those expected for the established magnon-electron relaxation mechanism in ferromagnetic metals. The critical mode (CM) response also follows from the nature of the thin film spin wave dispersion band. These CM profiles are quite different from those found for spin wave instability processes in ferrites. The results show clearly that nonlinear spin waves play a critical role in high power thin film precession dynamics.

ACKNOWLEDGMENTS

This work was supported in part by the National Science Foundation, Grant No. DMR-0108797, the United States Office of Naval Research, Grant No. N00014-94-1-0096, the U.S. Army Research Office, Grant No. DAAD19–02–1–0197, the National Institute of Standards and Technology (NIST) Nanomagnetodynamics Program, and the Information Storage Industry Consortium (INSIC) Ultra High Density Recording (EDHR) program. Dr. H. Pascard, previously affiliated with the Centre Nationale de Recherche Scientifique, Bellevue, France, and Dr. F. Ono, previously affiliated with Tohoku University, Sendai, Japan, provided the Permalloy films used in this work. Dr. R. D. McMichael and Dr. P. Kabos are acknowledged for a critical reading of the manuscript and perceptive editorial comments.

APPENDIX

This appendix gives working equations for the first order spin wave instability coupling coefficient $W_k^{(1)}$ needed for the h_{crit} analysis given in Sec. IV C. This $W_k^{(1)}$ may be written as

$$W_k^{(1)} = (1 - N_k)\sin\,\theta_k \cos\,\theta_k \times \{(A_k - B_k + \omega_p/2)q_{LA} + (A_k - B_k - \omega_p/2)q_{AL}^*\}. \quad \text{(A1)}$$

The A_k and B_k functions are given by

$$A_k = \omega_H + |\gamma| D k^2 + \tfrac{1}{2}\omega_M[(1 - N_k)\sin^2\,\theta_k + N_k] \quad \text{(A2)}$$

and

$$B_k = \tfrac{1}{2}\omega_M[(1 - N_k)\sin^2\,\theta_k - N_k]. \quad \text{(A3)}$$

Downloaded 06 Sep 2004 to 150.134.221.6. Redistribution subject to AIP license or copyright, see http://jap.aip.org/jap/copyright.jsp

The ω_H parameter in the A_k and B_k expressions is equal to $|\gamma|H$ and expresses the field in frequency units. The q_{LA} and q^*_{AL} denote, respectively, Larmor and anti-Larmor uniform mode response functions for a linearly polarized in plane microwave field and Gilbert damping

$$q_{\mathrm{LA}} = \frac{\omega_H + \omega_M + \omega_p[1 + i2\eta_0/(2\omega_H + \omega_M)]}{\omega_0^2 - \omega_p^2 + i2\omega_p\eta_0}, \tag{A4}$$

$$q^*_{\mathrm{AL}} = \frac{\omega_H + \omega_M - \omega_p[1 + i2\eta_0/(2\omega_H + \omega_M)]}{\omega_0^2 - \omega_p^2 + i2\omega_p\eta_0}. \tag{A5}$$

In the above, $\omega_0 = \sqrt{\omega_H(\omega_M + \omega_H)}$ is the uniform mode FMR frequency. The uniform mode relaxation rate η_0 is connected to the FMR linewidth ΔH_0 through the relation

$$\eta_0 = \frac{|\gamma|^2}{4}\frac{2H_{\mathrm{res}} + 4\pi M_s}{\omega_0}\Delta H_0. \tag{A6}$$

[1]T. J. Silva, P. Kabos, and M. R. Pufall, Appl. Phys. Lett. **81**, 2205 (2002).
[2]J. P. Nibarger, R. Lopusnik, and T. J. Silva, Appl. Phys. Lett. **82**, 2112 (2003).
[3]R. W. Damon, Rev. Mod. Phys. **25**, 239 (1953).
[4]N. Bloembergen and S. Wang, Phys. Rev. **93**, 72 (1954).
[5]H. Suhl, J. Phys. Chem. Solids **1**, 209 (1957).
[6]E. Schloemann, Technical Report No. R-48, 1959 (unpublished).
[7]A. J. Berteaud and H. Pascard, J. Appl. Phys. **37**, 2035 (1966).
[8]K. J. Harte, J. Appl. Phys. **36**, 960 (1965).
[9]J. B. Comly, T. Penney, and R. V. Jones, J. Appl. Phys. **34**, 1145 (1963).
[10]C. E. Patton and F. B. Humphrey, J. Appl. Phys. **37**, 4269 (1966).
[11]C. E. Patton, F. Ono, and M. Takahashi, IEEE Trans. Magn. **7**, 760 (1971).
[12]R. G. Cox, C. E. Patton, M. A. Wittenauer, P. Kabos, and L. Chen, J. Appl. Phys. **89**, 4454 (2001).
[13]A. V. Nazarov, R. G. Cox, and C. E. Patton, J. Appl. Phys. **92**, 3890 (2002).
[14]C. E. Patton, *Microwave Resonance and Relaxation*, edited by D. J. Craik (Wiley, London, 1975), Chap. 10.
[15]M. Chen and C. E. Patton, *Nonlinear Phenomena and Chaos in Magnetic Materials*, edited by P. E. Wigen (World Scientific, Singapore, 1994), Chap. 3.
[16]A. V. Nazarov, C. E. Patton, R. G. Cox, L. Chen, and P. Kabos, J. Magn. Magn. Mater. **248**, 164 (2002).
[17]O. G. Vendik, B. A. Kalinikos, and D. N. Chatorizhskiĭ, Fiz. Tverd. Tela (Leningrad) **19**, 387 (1977) [Sov. Phys. Solid State **19**, 22 (1977)]. Note that Eq. (19), among others, contains errors.
[18]C. E. Patton, J. Appl. Phys. **39**, 3060 (1968).
[19]K. J. Harte, J. Appl. Phys. **39**, 1503 (1968).
[20]R. Arias and D. L. Mills, Phys. Rev. B **60**, 7395 (1999).
[21]R. D. McMichael and P. Krivosik, IEEE Trans. Magn. **40**, 2 (2004).
[22]B. A. Kalinikos, N. G. Kovshikov, and N. V. Kozhus', Fiz. Tverd. Tela (Leningrad) **27**, 2794 (1985) [Sov. Phys. Solid State **27**, 1681 (1985)].
[23]R. E. DeWames and T. Wolfram, J. Appl. Phys. **41**, 987 (1970).
[24]B. A. Kalinikos and A. N. Slavin, J. Phys. C **19**, 7013 (1986).
[25]M. Nisenoff and R. W. Terhune, J. Appl. Phys. **36**, 732 (1965).
[26]M. Sparks, *Ferromagnetic Relaxation Theory* (McGraw-Hill, New York, 1964).

Downloaded 06 Sep 2004 to 150.134.221.6. Redistribution subject to AIP license or copyright, see http://jap.aip.org/jap/copyright.jsp